1 *S*-matrix theory of nonsequential double ionization

C. Figueira de Morisson Faria[1], X. Liu[2], and W. Becker[3]

[1] School of Engineering and Mathematical Sciences, City University, London EC1V OHB, UK C.F.M.Faria@city.ac.uk
[2] Department of Physics, Texas A & M University, College Station, TX 77843-4242, USA xjliu@neo.tamu.edu
[3] Max-Born-Institut, 12489 Berlin, Germany wbecker@mbi-berlin.de

1.1 Introduction

Atoms exposed to intense laser fields may be multiply ionized. Along the simplest pathway, this happens step by step. However, already more than twenty years ago, evidence was mounting for the contribution of a different pathway whereby two electrons are freed in one coherent process [1]. Clearly, this requires that the participating two electrons be correlated. Regardless of the detailed mechanism, this process is referred to as nonsequential double ionization (NSDI); for reviews, see [2].

The information provided by the highly differential cross sections that have been obtained with the help of the reaction-microscope technique [3–5] has largely terminated the debate about the physical mechanism responsible for NDSI: For the situation explored in most experiments, that is, high-intensity low-frequency lasers typified by the titanium-sapphire laser ($\lambda \approx 800$ nm) at 10^{14} to 10^{15} Wcm^{-2}, consensus has developed that NSDI is caused by the rescattering mechanism: an electron that is freed by tunneling ionization is driven by the laser field into a recollision with its parent ion. This is the same mechanism that is responsible, for example, for high-order harmonic generation and high-order above-threshold ionization [6]. Exactly how the up to the recollision inactive electron is freed is less clear and appears to depend, moreover, on the specific atom: the rare gases neon on the one hand and helium and argon on the other display distinctly different behavior [2].

The fact that the recollision pathway appears to be the first stage of NSDI will make possible future investigations that will explore the temporal evolution of the ionization dynamics. These rely on the fact that the time interval within the laser cycle during which the first electron is driven into the recollision is rather narrow. It is revealed by the momentum of the doubly charged ion, which is measured by the reaction microscope [7]. This technique, referred to as "streaking", has already been employed to elucidate various features of the single-ionization dynamics [8].

Various theoretical approaches have tried to advance the understanding of NSDI. The solution of the time-dependent Schrödinger equation in one spatial dimension has provided a great deal of insight [9], but in three spatial

dimensions it is extremely demanding and, in any event, its applicability is restricted to the simplest rare-gas atom, viz. helium [10]. Classical-trajectory methods that pursue electrons injected into the continuum by tunneling ionization have successfully reproduced many features of the data [11]. It is also possible, for a given scenario of how NSDI evolves, to identify the leading Feynman diagrams that contribute to the transition amplitude [12] (this work is reviewed in [13]) and to compute them by various methods [14–17]. This review is concerned with the latter approach, which is fully quantum mechanical from the outset, but suggests a straightforward classical limit, which is very easy to compute. The latter has been shown to reproduce the quantum results with high accuracy provided the laser intensity is high enough [18].

In section 1.2 we introduce the basic rescattering–impact-ionization S-matrix element whose detailed investigation is at the focus of this review. In subsection 1.2.1 we sketch its evaluation with saddle-point methods. This leads to a discussion of the classical kinematics underlying the S-matrix description. Various classical concepts related to the "simple-man model" are also briefly reviewed in this section. We also draw attention to the fact that the S-matrix element depends on the gauge used in coupling the charged particles to the laser field. In subsections 1.2.3 and 1.2.4 we briefly discuss other scenarios for NSDI. The consequences of the choice of the crucial electron-electron interaction by which the returning electron ejects the bound electron is reviewed in section 1.3. Further possible refinements of the theory include the exact introduction of electron-electron repulsion in the final state (section 1.4) and the detailed consideration of the initial bound states (section 1.5). The classical limit of the S-matrix element considered is discussed and compared with the fully quantum-mechanical results in section 1.6. We then make use of the classical description in the discussion of NSDI by few-cycle pulses (section 1.7) and nonsequential multiple ionization (section 1.8). Throughout the paper, we make frequent contact with experimental results.

1.2 The S-matrix element of the rescattering–impact-ionization scenario

In the rescattering scenario, NSDI is initiated by one electron tunneling to freedom through the potential barrier created by the binding potential and the scalar potential of the intense laser field. When the electron is driven back to its parent ion by the oscillating laser field, it may in the recollision process dislodge another electron (or several electrons). The Feynman diagram that describes the simplest such mechanism is shown in panel (a) of figure 1.1: the returning electron frees the bound electron through a single interaction mediated by the potential V_{12}. The corresponding transition amplitude is

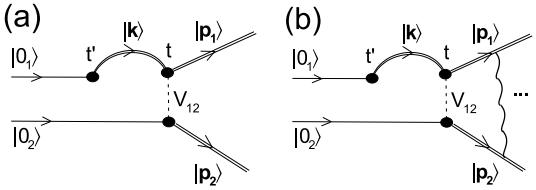

Fig. 1.1. Feynman diagrams corresponding to the transition amplitude (1.1), (a) without and (b) with electron-electron repulsion between the two electrons in the final state. The vertical wavy line and the dots in (b) indicate the Coulomb interaction, which is exactly accounted for by the two-electron Volkov solution. The dashed vertical line represents the electron-electron interaction V_{12} by which the second electron is set free

$$M_{\boldsymbol{p_1 p_2}} = -\int_{-\infty}^{\infty} \mathrm{d}t \int_{-\infty}^{t} \mathrm{d}t' \langle \psi^{(\mathrm{V})}_{\boldsymbol{p_1 p_2}}(t)|V_{12} U_1^{(\mathrm{V})}(t,t') V_1 U_2^{(0)}(t,t')|\psi_0(t')\rangle, \tag{1.1}$$

where V_1 and $U_1^{(\mathrm{V})}(t,t')$ denote the atomic binding potential and the Volkov time-evolution operator acting on the first electron, $U_2^{(0)}(t,t')$ is the field-free propagator acting on the second electron, and V_{12} is the electron-electron interaction through which the second electron is freed by the first. For the initial bound state $|\psi_0(t')\rangle$, a product of one-electron states $|\psi_0^{(n)}(t')\rangle = e^{i|E_{0n}|t'}|\psi_0^{(n)}\rangle$ with ionization potentials $|E_{0n}|$ is adopted. In this section, the final electron state with asymptotic momenta $\boldsymbol{p}_1$ and $\boldsymbol{p}_2$ is taken as the symmetrized[4] product state of one-electron Volkov states[5],

$$\langle \boldsymbol{r}|\psi^{(\mathrm{V})}_{\boldsymbol{p}}(t)\rangle = (2\pi)^{-3/2} \exp\{\mathrm{i}[\boldsymbol{p} + \boldsymbol{A}(t)]\cdot\boldsymbol{r}\} \exp\left(\frac{-\mathrm{i}}{2}\int^{t} \mathrm{d}\tau [\boldsymbol{p} + \boldsymbol{A}(\tau)]^2\right). \tag{1.2}$$

We use the length gauge and employ atomic units throughout. Below, we will also consider a two-electron Volkov state, which exactly incorporates the Coulomb repulsion between the two electrons [22]. The physical assumptions underlying the amplitude (1.1) correspond to the so-called strong-field approximation (SFA), which was developed for strong-field ionization [23, 24] and high-order harmonic generation [25]. Briefly, for atomic bound states their interaction with the laser field is neglected, and for continuum states their interaction with the atomic (or ionic) binding potential. A systematic derivation of the amplitude (1.1) can be found in [12].

For the computation of the amplitude (1.1), the Volkov time-evolution operator is usually expanded in terms of the Volkov states (1.2),

[4] For a discussion of symmetry vs. antisymmetry if spin is included, see [19, 20].

[5] A Volkov state is obtained from the solution of the time-dependent Schrödinger equation for a free particle in an external plane-wave laser field. Such states were first derived by Volkov, in a relativistic context [21].

$$U^{(\mathrm{V})}(t,t') = \int \mathrm{d}^3\boldsymbol{k} |\psi_{\boldsymbol{k}}^{(\mathrm{V})}(t)\rangle\langle\psi_{\boldsymbol{k}}^{(\mathrm{V})}(t')|. \tag{1.3}$$

As a result, the amplitude (1.1) has the form

$$M_{\boldsymbol{p}} = -\int_{-\infty}^{\infty} \mathrm{d}t \int_{-\infty}^{t} \mathrm{d}t' \int \mathrm{d}^3\boldsymbol{k} V_{\boldsymbol{p}\boldsymbol{k}} V_{\boldsymbol{k}0} \exp[\mathrm{i}S_{\boldsymbol{p}}(t,t',\boldsymbol{k})], \tag{1.4}$$

with the action

$$S_{\boldsymbol{p}}(t,t',\boldsymbol{k}) = -\frac{1}{2}\left[\sum_{n=1}^{2}\int_{t}^{\infty} \mathrm{d}\tau[\boldsymbol{p}_n + \boldsymbol{A}(\tau)]^2 + \int_{t'}^{t} \mathrm{d}\tau[\boldsymbol{k} + \boldsymbol{A}(\tau)]^2\right] + |E_{01}|t' + |E_{02}|t. \tag{1.5}$$

Here $\boldsymbol{A}(t)$ denotes the vector potential of the laser field, $\boldsymbol{p} \equiv (\boldsymbol{p}_1, \boldsymbol{p}_2)$ the final electron momenta, and $\boldsymbol{k}$ the drift momentum of the first electron in between ionization and recollision. The binding potential V_1 of the first electron and the electron-electron interaction V_{12} enter (1.4) through their form factors

$$V_{\boldsymbol{p}\boldsymbol{k}} = \langle \boldsymbol{p}_2 + \boldsymbol{A}(t), \boldsymbol{p}_1 + \boldsymbol{A}(t)|V_{12}|\boldsymbol{k} + \boldsymbol{A}(t), \psi_0^{(2)}\rangle \tag{1.6}$$

and

$$V_{\boldsymbol{k}0} = \langle \boldsymbol{k} + \boldsymbol{A}(t')|V_1|\psi_0^{(1)}\rangle. \tag{1.7}$$

Various choices have been made for the binding potential V_1 (and the corresponding wave functions) and the interaction V_{12}, which will be discussed below. If the former is described by a regularized zero-range potential so that $V_1(\boldsymbol{r}) \sim \delta(\boldsymbol{r})(\partial/\partial r)r$ and the latter by a three-body contact potential $V(\boldsymbol{r}_1, \boldsymbol{r}_2) \sim \delta(\boldsymbol{r}_1 - \boldsymbol{r}_2)\delta(\boldsymbol{r}_2)$, then the amplitude (1.1) can be reduced to a one-dimensional quadrature involving Bessel functions [26]. Most of the time, for the binding potential V_1 a Coulomb potential and for the wave functions $\psi_0^{(i)}(\boldsymbol{r})$ ground-state hydrogenic wave functions have been adopted, while different forms of the interaction V_{12} have been investigated. This will be discussed in section 1.3.

1.2.1 Saddle-point approximations and basic concepts

For arbitrary potentials, given the low frequencies and high intensities employed in current experiments, for the numerical evaluation of the amplitude (1.1) in the form (1.4) the method of steepest descent [also known as the saddle-point approximation (SPA)] is the method of choice. Thus, we must determine the values of $\boldsymbol{k}$, t', and t for which the action $S_{\boldsymbol{p}}(t,t',\boldsymbol{k})$ is stationary, so that its partial derivatives with respect to these variables vanish. This condition gives the equations

$$[\boldsymbol{k} + \boldsymbol{A}(t')]^2 = -2|E_{01}|, \tag{1.8a}$$

$$\sum_{n=1}^{2} [\boldsymbol{p}_n + \boldsymbol{A}(t)]^2 = [\boldsymbol{k} + \boldsymbol{A}(t)]^2 - 2|E_{02}|, \tag{1.8b}$$

$$\int_{t'}^{t} \mathrm{d}\tau\, [\boldsymbol{k} + \boldsymbol{A}(\tau)] = 0. \tag{1.8c}$$

Equations (1.8a) and (1.8b) express energy conservation at the ionization and rescattering times, respectively, while (1.8c) determines the intermediate momentum of the first electron so that it returns to the ion. Obviously, the solutions t'_s ($s = 1, 2, \dots$) of (1.8a) cannot be real. Hence, t_s and $\boldsymbol{k}_s$ are complex, too.

In the standard SPA, the action (1.5) in the matrix element (1.4) is expanded to second order about the solutions to the saddle-point equations (1.8), whereupon the integrations can be carried out with the result

$$M^{(\mathrm{SPA})} = \sum_s A_s \exp(\mathrm{i}S_s), \tag{1.9a}$$

$$S_s = S_{\boldsymbol{p}}(t_s, t'_s, \boldsymbol{k}_s), \tag{1.9b}$$

$$A_s = (2\pi\mathrm{i})^{5/2} \frac{V_{\boldsymbol{p}\boldsymbol{k}_s} V_{\boldsymbol{k}_s 0}}{\sqrt{\det S''_{\boldsymbol{p}}(t, t', \boldsymbol{k})|_s}}. \tag{1.9c}$$

Here the index s runs over the *relevant* saddle points, those that are visited by an appropriate deformation of the real integration contour, which is the real five-dimensional $(t, t', \boldsymbol{k})$ space, to complex values, and $S''_{\boldsymbol{p}}(t, t', \boldsymbol{k})|_s$ denotes the five-dimensional matrix of the second derivatives of the action (1.5) with respect to t, t' and $\boldsymbol{k}$, evaluated at the saddle points. The time dependence of the form factors (1.6) and (1.7) is considered as slow, unless stated otherwise (see section 1.5 and [27]).

The SPA requires that the various saddle points be well separated. This is not always satisfied in the present case nor in intense-laser atom problems, in general. In order to see this, we must have a closer look at the solutions of the saddle-point equations (1.8).

The classically allowed regime

Equation (1.8b) describes energy conservation in the rescattering process. From the point of view of the first electron, rescattering is inelastic, since it donates energy to the second electron. Let us ignore, for the moment, the ionization potential $|E_{01}|$ and consider linear polarization. Then, $\boldsymbol{k} = -\boldsymbol{A}(t')$, and $\boldsymbol{k}$ and t' are real. For given t', (1.8a) and (1.8c) then yield the rescattering time t and the momentum $\boldsymbol{k}$. In the space of the final momenta $\boldsymbol{p} = (\boldsymbol{p}_1, \boldsymbol{p}_2)$, (1.8b) is the equation of the surface of a six-dimensional sphere with its center at $(-\boldsymbol{A}(t), -\boldsymbol{A}(t))$ and its squared radius given by $[\boldsymbol{k}+\boldsymbol{A}(t)]^2 - 2|E_{02}|$. We only consider times t' such that the latter is positive. Then all possible

electron momenta $\boldsymbol{p}$ that are classically accessible in the process where the first electron is ionized at the time t' are located on the surface of this sphere.

The union of all these spheres upon variation of the ionization time t' contains all final electron momenta that are in this sense classically accessible. Below, we will frequently refer to it as the "classically allowed region". Leaving this region along any path in the $(\boldsymbol{p}_1, \boldsymbol{p}_2)$ space, the NSDI yield experiences a sharp "cutoff". Quantum mechanics allows a nonzero yield outside the classically allowed region, which, however, decreases exponentially with increasing distance from its boundary. Formally, this is accomplished by the fact that the exact solutions of the saddle-point equations (1.8), which are always complex, exhibit rapidly increasing imaginary parts [28].

Saddle-point solutions come in pairs

Since the saddle-point equations (1.8) are real, for any given solution its complex conjugate is a solution as well. Let us consider a laser field represented by an infinitely extended monochromatic plane wave. For given $\boldsymbol{p}_1$ and $\boldsymbol{p}_2$ and for the rescattering time $\mathrm{Re}\, t$ restricted to some period of the field, say $nT < \mathrm{Re}\, t \leq (n+1)T$, there are infinitely many solutions whose ionization times $\mathrm{Re}\, t'$ extend further and further into the past ($\mathrm{Re}\, t' < \mathrm{Re}\, t$). A general classification of these solutions and their significance for ATI and NSDI can be found in [29]. The solutions generally come in pairs (plus their complex conjugates); for a general discussion of this issue, see [30]. Here, we will consider the pair of solutions $t_s, t'_s, \boldsymbol{k}_s$ $(s = i, j)$ having the shortest "travel times" $\mathrm{Re}\,(t_s - t'_s)$. Let us suppose that the solutions $s = i, j$ (rather than their complex conjugates) are the relevant solutions as defined above inside the classical region so that they have to be included into the sum (1.9a). Usually (but not always [29]), the contributions of the other pairs can be neglected. Outside the classical region, with increasing distance from its boundary both solutions of the pair develop quickly increasing imaginary parts, and one or the other must be discarded from the sum lest it explode exponentially [30]. This transition occurs very rapidly. It is illustrated in figure 1.2, which shows that the two saddle points approach each other very closely near the classical cutoff. Actually, figure 1.2 is for the closely related but simpler case of ATI. Corresponding illustrations for NSDI are discussed in [28]. The procedure of discarding one solution at some point is to some extent arbitrary and may lead to the artifact of a spike in the yield. This is due to the fact that the SPA is not applicable when two solutions approach each other too closely.

A convenient solution to this problem is provided by a certain uniform approximation [30], which is designed to deal with pairs of solutions and automatically takes care of the "discarding". The result requires the same input as (1.9), namely the action and its second derivatives at the saddle points, and is hardly more complicated. Within the classically allowed region, it is

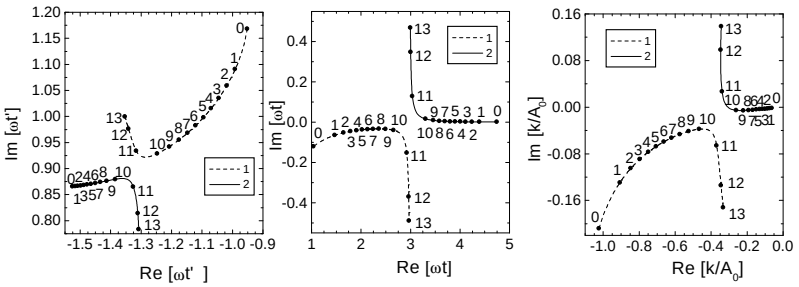

Fig. 1.2. Complex saddle points t_s' (left panel), t_s (middle panel, and k_{xs} $(s = i, j)$ (right panel) for the pair of solutions having the shortest travel times as discussed in the text. The figure is for ATI, for a Keldysh parameter of $\gamma = 0.975$, and emission parallel to the laser field. The panels present the paths in the complex plane that are followed by the saddle points as a function of the final energy of the electron at the detector, which is indicated by the numbers (in multiples of U_p). The figure shows how the saddle points of a pair approach each other very closely near the classical cutoff at $10\,U_p$, which is the classical cutoff of the ATI energy spectrum. The contribution of the orbit that is drawn dashed has to be dropped after the cutoff. From [30]

$$
\begin{aligned}
M_{i+j} &= \sqrt{2\pi \Delta S/3}\exp(\mathrm{i}\bar{S} + \mathrm{i}\pi/4)\left\{\bar{A}[J_{1/3}(\Delta S) + J_{-1/3}(\Delta S)]\right. \\
&\quad \left. + \Delta A[J_{2/3}(\Delta S) - J_{-2/3}(\Delta S)]\right\}, \qquad (1.10)\\
\Delta S &= (S_i - S_j)/2, \qquad \bar{S} = (S_i + S_j)/2, \\
\Delta A &= (A_i - \mathrm{i}A_j)/2, \quad \bar{A} = (\mathrm{i}A_i - A_j)/2.
\end{aligned}
$$

The noninteger Bessel functions have to be analytically continued when the parameters move into the nonclassical region. For details we refer to [30].

Classical cutoffs

If in (1.8a) the first ionization potential E_{01} is neglected, the electron starts its orbit in the continuum with an initial velocity $\boldsymbol{v}(t') \equiv \boldsymbol{k} + \boldsymbol{A}(t') = \boldsymbol{0}$ and t, t', and $\boldsymbol{k}$ are all real inside the classically allowed region. The classical boundary then is characterized by the fact that the two solutions of the afore-mentioned pair merge. (There are no such real solutions outside the classically allowed region). This can be exploited to obtain (approximate) closed formulas for the cutoffs (corresponding to the well known cutoff $|E_0| + 3.17U_p$ for high-order harmonic generation); see [31].

Electron kinematics in the laser field: the "simple-man model"

An electron released at the time t with zero velocity in a laser field with vector potential $\boldsymbol{A}(t)$, such that outside the laser pulse $\boldsymbol{A}(-\infty) = \boldsymbol{A}(\infty) = \boldsymbol{0}$, will reach the detector (outside the pulse) with momentum

$$\boldsymbol{p} = -\boldsymbol{A}(t). \tag{1.11}$$

This simple relation follows from the fact that in a laser field that only depends on time the electron velocity is given by $\boldsymbol{v}(t) \equiv \boldsymbol{p} + \boldsymbol{A}(t)$ with constant $\boldsymbol{p}$. If the temporal average of the vector potential vanishes, $\langle \boldsymbol{A} \rangle_t = \boldsymbol{0}$, then $\boldsymbol{p}$ is the drift momentum of the electron, which is conserved when the laser pulse leaves the electron behind. The relation (1.11) sets the benchmarks for the electron and ion spectra observed in NSDI. For tunneling ionization, it implies that the electron's momentum at the detector is bound by $|\boldsymbol{p}| \leq \max_t |\boldsymbol{A}(t)| = 2\sqrt{U_p}$. For NSDI, higher momenta are classically possible, since the returning electron generally has some energy left after it dislodged the bound electron and may share it with the latter. The situation easiest to analyze is when the energy of the returning electron is just sufficient to remove the bound electron. In this case, both electrons will be released into the continuum with zero kinetic energy near a zero crossing of the electric field (since an electron returning around this time has maximal energy). Both electrons then will reach the detector with momenta near $2\sqrt{U_p}$. If the momentum of the laser photons is small enough that it can be ignored, momentum conservation implies

$$P_{\max} = 4\sqrt{U_p} \tag{1.12}$$

for the momentum of the doubly ionized ion. For higher intensities, such that the energy of the returning electron is amply sufficient to accomplish the second ionization, the above values roughly predict the *centers* of the electron and the ion momentum distributions, as will be seen below.

The choice of gauge

The strong-field approximation, on which the present formalism relies, is not gauge invariant; see. e.g. [32]. This problem has been present not only for NSDI, but for all strong-field phenomena, such as above-threshold ionization and high-order harmonic generation, when they are treated via the SFA. In the nonrelativistic regime where the long-wavelength approximation can be used, the laser-matter interaction operator is $\boldsymbol{r} \cdot \boldsymbol{E}(t)$ in length gauge and $\hat{\boldsymbol{p}} \cdot \boldsymbol{A}(t) + \frac{1}{2}\boldsymbol{A}^2(t)$ in velocity gauge. Of the seminal papers, [23] employed length gauge while [24] used velocity gauge. In NSDI S-matrix calculations, references [14] rely on velocity gauge and [16, 17] on length gauge. Only for contact potentials are identical results obtained in different gauges. For an electron bound by a short-range potential (as is the case for a negative ion), comparison of the SFA with the numerical solution of the time-dependent Schrödinger equation has shown that in this case the length gauge yields superior results [32, 33].

For the S-matrix calculations of NSDI, the question of which gauge to use within the SFA is open. The difference between the two gauges enters via the spatial part of the Volkov solution (1.2), which is $\exp\{\mathrm{i}[\boldsymbol{p} + \boldsymbol{A}(t)] \cdot \boldsymbol{r})\}$

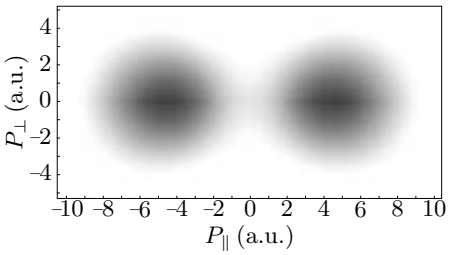

Fig. 1.3. Linear-scale density plot of the distribution of the ion momentum $\boldsymbol{P} = (P_\parallel, P_\perp)$ in nonsequential double ionization of neon at 8×10^{14} W/cm^2 and $\hbar\omega = 1.55$ eV. From [26]

in length gauge versus $\exp\{\mathrm{i}\boldsymbol{p}\cdot\boldsymbol{r}\}$ in velocity gauge. Thus, in length gauge, the form factors (1.6) and (1.7) depend on the *instantaneous momenta* at the time of rescattering and ionization while in velocity gauge they depend on the *drift momenta*. Specifically, in (1.6), the $\boldsymbol{A}(t)$'s are absent in velocity gauge, which invalidates the mechanism described below equation (1.21). This leads to momentum distributions that, in comparison with length gauge, are more concentrated near the diagonal $p_{1\parallel} = p_{2\parallel}$ and the origin $p_{1\parallel} = p_{2\parallel} = 0$ [14].

1.2.2 Ion-momentum distributions

The reaction-microscope technique is capable of measuring a fully (sixfold) differential cross section, by detecting the three-dimensional momenta of two particles of opposite charge, viz. the ion and one electron. Such a fully differential measurement was recently accomplished [7]. However, the very first experiments were content with recording the NSDI yield as a function of two momentum components of the ion, one parallel ($P_\parallel$) and one transverse ($P_\perp$) to the linearly polarized laser field, while the second transverse component ($P_{\perp,2}$) was integrated over. In terms of the amplitude (1.1), this corresponds to the momentum distribution

$$F(P_\parallel, P_\perp) = \int \mathrm{d}P_{\perp,2} \int \mathrm{d}^3\boldsymbol{p}_1 \mathrm{d}^3\boldsymbol{p}_2 \delta(\boldsymbol{P} - \boldsymbol{p}_1 - \boldsymbol{p}_2) |M_{\boldsymbol{p_1 p_2}}|^2. \tag{1.13}$$

Figure 1.3 shows such a distribution evaluated for the conditions of [4]. In the calculation, all potentials were taken as contact potentials. As expected from (1.12), the ion-momentum distribution peaks near $P_{\max} = 5.3$ a.u., $\boldsymbol{P}_\perp = 0$. Electrons can acquire momenta higher than allowed by (1.11) for two reasons: (i) they can start with a nonzero velocity, and (ii) quantum mechanics allows momenta in excess of (1.11). By overall momentum conservation, the ion momentum then may also exceed the bound (1.12) and, indeed, figure 1.3 shows that it does.

Figure 1.4 exhibits distributions of the longitudinal component of the ion momentum for argon, helium, and neon, calculated under the same conditions

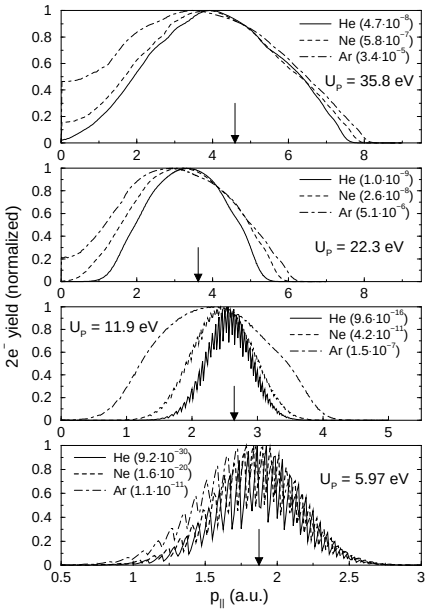

Fig. 1.4. Distribution of $P_\parallel$ for $\boldsymbol{P}_\perp = 0$ for He, Ne, and Ar, $\hbar\omega = 1.55$ eV, and various intensities characterized by the corresponding ponderomotive potential U_p. Because of symmetry, the distribution is only shown for $P_\parallel > 0$. Each curve has been normalized to a maximum of unity; the number given in parentheses for each curve specifies the respective normalization factor. The vertical arrows mark the position of $4\sqrt{U_p}$; cf. equation (1.12). From [15]

as figure 1.3 for various laser intensities. It illustrates a general tendency of the amplitude (1.1), namely, for decreasing intensity and increasing ionization potential (that means, towards the classical boundary and beyond) the ion-momentum distribution concentrates more and more near the value (1.12). At the same time, the yield drops steeply. Both features, the narrowing and the steeply decreasing yield, are present in the data, but to a lesser degree. Indeed, the widths of the two humps stay almost the same when due to decreasing intensity the process moves out of the classical region [34].

1.2.3 Rescattering-excitation scenario

The measured ion-momentum distributions of neon on the one hand and helium and argon on the other [and also the electron momentum correlations to be considered below, cf. (1.20)] are very different. For neon, in contrast to helium and argon, the region about $P_\parallel = 0$ is largely depopulated. This becomes even more pronounced when the distribution of the electron momenta $p_{i\parallel}\,(i = 1, 2)$ parallel to the laser-field polarization is plotted [cf. equation (1.20) below]. For neon, it concentrates in the first and third quadrant [4,35].

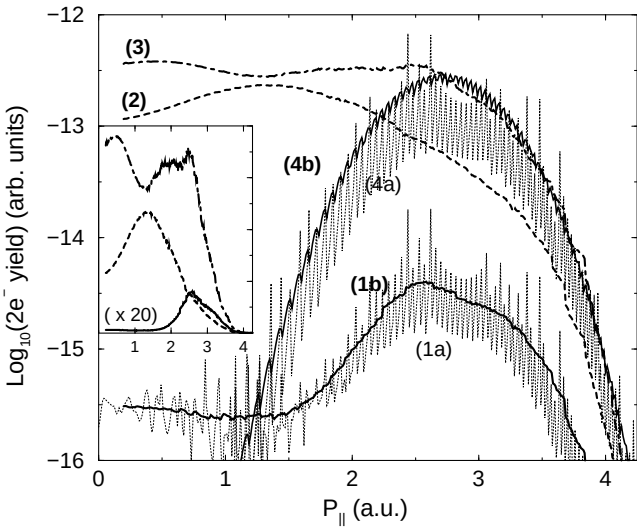

Fig. 1.5. Log-scale distribution of the total momentum in double ionization of helium for $U_p = 14$ eV based on the assumption that the returning electron promotes the bound electron into an excited state with energy $E^*_{02} = -0.5$, -0.22, -0.125 a.u., for curves (1), (2), and (3), respectively. The calculation is in one dimension only. The curves (4) display, for comparison, the distribution generated by the direct rescattering scenario of equation (1.1) for contact interactions; (4b) was calculated in three dimensions and (4a) in one. The spiky structures of curves (4a) and (1a) are due to channel closings, which have a more pronounced effect in one than in three dimensions. Curves (1b), (2), and (3) are smoothed so as to suppress these effects, curve (1a) is not. The inset redraws curves (1b), (2), and (3) on a linear scale for easier comparison with the data [3]. From [15]

This is not observed for helium and argon, which exhibit a sizable population in the second and fourth quadrant [3]. Consensus has developed that for the latter rare gases another mechanism significantly contributes [5]: the recolliding electron promotes the bound electron to some excited state from which it tunnels out at a later time, usually near a maximum of the laser field so that its drift momentum will be low [cf. (1.11)]. Indeed, this mechanism has been confirmed by a calculation of the cross section for impact ionization and impact excitation in electron-ion collisions [36]. The latter was found to be exceptionally low for neon. The basic features of recollision excitation follow from an amplitude such as (1.1) with, however, integration over one additional time: the first electron tunnels out at the time t'', recollides, promotes the bound electron into an excited state with energy $E^*_{02} > E_{02}$, and leaves the interaction region at the time $t' > t''$, while the bound electron only becomes free at the later time $t > t'$. Figure 1.5 exhibits the results of

such a model. Indeed, for a sufficiently high-lying excited state, the region around zero ion momentum is filled in.

1.2.4 Other scenarios

Before the advent of the reaction microscope established the strong dominance of the recollision pathway, various other scenarios had been discussed. While none of them seems to be relevant for the recent experiments with rare gases and high-intensity Ti:Sa lasers, they might well turn out to contribute in other regimes, such as provided by high-frequency free-electron lasers. One mechanism that originally was expected to contribute is the so-called shake-off where the ion rearranges itself after one electron has been suddenly removed and ejects a second electron in the process; see, e.g., [2]. This is closely related to the so-called two-step-one process where the first electron on its way out shares energy with a second still bound electron enabling the latter to become free as well. Finally, double tunneling is a fascinating scenario [37], which is all but certain to play a role in systems such as H^- where a very large disparity exists between the detachment energy of 0.75 eV of the first electron and the binding energy of 13.6 eV of the subsequent hydrogen atom. Simple estimates using the quasistatic tunneling rate (1.26) show that it is much more favorable for the two electrons to tunnel out in one joint effort than sequentially one at a time, and this is confirmed by more elaborate calculations [38]. The big impediment for an experimental verification is the fact that laser pulses with extremely high contrast are required in order that a sufficient number of H^- ions survive into the peak of the pulse.

1.3 The electron-electron interaction V_{12}

More recent experiments have recorded the distribution of the longitudinal momenta $p_{1\parallel}$ and $p_{2\parallel}$ of the two electrons, with the remaining transverse components either entirely integrated over or restricted to certain intervals [35,39]. These "correlation" distributions carry much more information about the NSDI dynamics than the ion-momentum distributions discussed above. For example, it is easy to envision identical ion-momentum distributions that correspond to very different correlations. In particular, the correlations very clearly display the consequences of the choice of the crucial electron-electron interaction V_{12} in the transition amplitude (1.1). We will review the effects of four different choices of this interaction, namely

$$V(\boldsymbol{r}_1, \boldsymbol{r}_2) \sim |\boldsymbol{r}_1 - \boldsymbol{r}_2|^{-1}, \tag{1.14a}$$

$$V(\boldsymbol{r}_1, \boldsymbol{r}_2) \sim \delta(\boldsymbol{r}_1 - \boldsymbol{r}_2)\delta(\boldsymbol{r}_2), \tag{1.14b}$$

$$V(\boldsymbol{r}_1, \boldsymbol{r}_2) \sim |\boldsymbol{r}_1 - \boldsymbol{r}_2|^{-1}\delta(\boldsymbol{r}_2), \tag{1.14c}$$

$$V(\boldsymbol{r}_1, \boldsymbol{r}_2) \sim \delta(\boldsymbol{r}_1 - \boldsymbol{r}_2). \tag{1.14d}$$

Of these, the pure electron-electron Coulomb interaction (1.14a) appears to be the obvious choice and, indeed has been widely used [12, 14, 16]. The electron-electron contact interaction (1.14b) which only acts if both electrons are at the position of the ion (in effect, a three-body contact interaction) has also been frequently employed [15]. Both interactions have been compared in various regards in [17,18,40]. More recently, the Coulomb interaction (1.14c), which is only effective if the second (bound) electron is located at the position of the ion, and the electron-electron contact interaction (1.14d), which is not restricted to the position of the ion, have also been studied [27]. The interactions (1.14b) and (1.14c) are *effective* three-body interactions, which attempt to take into account that the effective electron-electron interaction will depend on the positions of the electrons relative to the ion. An alternative interpretation, which formally leads to the same results, is to consider a two-body interaction V_{12} in (1.17) and a wave function $\langle \boldsymbol{r}|\psi_0^{(2)}\rangle$ in (1.18) that is extremely strongly localized at the position of the ion; for details, see [27].

We may write

$$V(\boldsymbol{r}_1, \boldsymbol{r}_2) = V_{\rm rel}(\boldsymbol{r}_1 - \boldsymbol{r}_2)U(\boldsymbol{r}_2), \tag{1.15}$$

where $U(\boldsymbol{r})$ is constant unless we allow for an effective interaction. The form factor (1.6) then is the product of two Fourier transforms:

$$V_{\boldsymbol{pk}} = [v(\boldsymbol{p}_1 - \boldsymbol{k}) + v(\boldsymbol{p}_2 - \boldsymbol{k})]u(\tilde{\boldsymbol{p}}), \tag{1.16}$$

where

$$v(\boldsymbol{p}_1 - \boldsymbol{k}) = \int \mathrm{d}^3\boldsymbol{r}\mathrm{e}^{\mathrm{i}(\boldsymbol{p}_1-\boldsymbol{k})\cdot\boldsymbol{r}}V_{\rm rel}(\boldsymbol{r}), \tag{1.17}$$

$$u(\tilde{\boldsymbol{p}}) = \int \mathrm{d}^3\boldsymbol{r}\mathrm{e}^{\mathrm{i}\tilde{\boldsymbol{p}}\cdot\boldsymbol{r}}U(\boldsymbol{r})\psi_0^{(2)}(\boldsymbol{r}), \tag{1.18}$$

and $\tilde{\boldsymbol{p}} = \boldsymbol{p}_1 + \boldsymbol{p}_2 - \boldsymbol{k} + \boldsymbol{A}(t)$ as above. Unless $U(\boldsymbol{r})$ is a contact interaction [as it is for (1.14b) and (1.14c)], the form factor will depend via (1.18) on the initial state of the second electron; see section 1.5. The Fourier transform (1.17) of the relative interaction between the two electrons depends on the momentum transfer $\boldsymbol{k} + \boldsymbol{A}(t) - [\boldsymbol{p}_1 + \boldsymbol{A}(t)] = \boldsymbol{k} - \boldsymbol{p}_1$ from the returning electron to the bound electron. If this interaction has Coulomb form, then

$$v(\boldsymbol{p}_1 - \boldsymbol{k}) \sim (\boldsymbol{p}_1 - \boldsymbol{k})^{-2}, \tag{1.19}$$

is the well-known Coulomb form factor. If, on the other hand, it has contact form, then $v(\boldsymbol{p}_1 - \boldsymbol{k}) = \text{const}$.

We shall calculate and discuss integrals of the type

$$D(p_{1\parallel}, p_{2\parallel}) = \int \mathrm{d}^2\boldsymbol{p}_{1\perp}\mathrm{d}^2\boldsymbol{p}_{2\perp}|M_{i+j}|^2, \tag{1.20}$$

where the integration extends over a certain range of the final transverse momenta, i.e. of their magnitudes and/or their relative orientation, and M_{i+j} is computed by the uniform approximation (1.10).

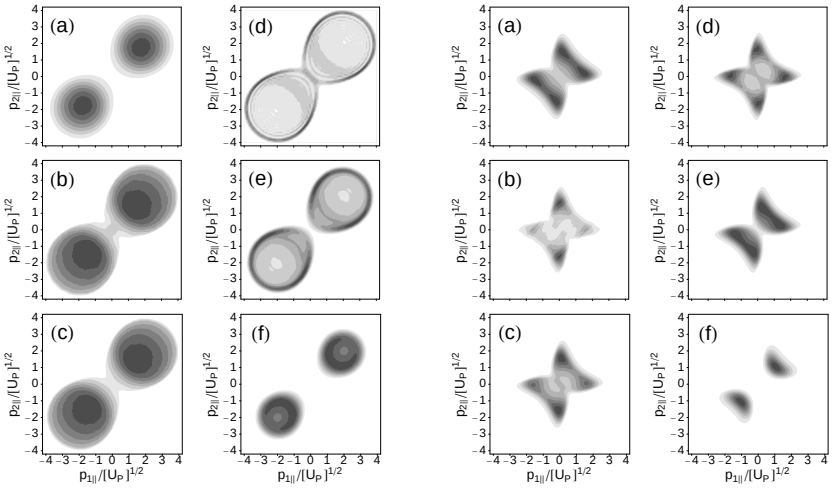

Fig. 1.6. Left-hand panels: Momentum correlation function (1.20) of the electron momenta parallel to the laser field for nonsequential double ionization computed with the uniform approximation using the contact interaction (1.14b). The field frequency is $\omega = 0.0551$ a.u. and the ponderomotive energy $U_P = 1.2$ a.u., which corresponds to an intensity of $5.5 \times 10^{14}\mathrm{W/cm}^2$. The first two ionization potentials are $|E_{01}| = 0.79$ a.u. and $|E_{02}| = 1.51$ a.u. corresponding to neon. Panel (a) shows the yield for the case where the transverse momenta $\boldsymbol{p}_{n\perp}$ $(n = 1, 2)$ are completely integrated over, whereas in the remaining panels they are restricted to certain intervals. In panels (b) and (c), $\boldsymbol{p}_{2\perp}$ is integrated, while $0 < p_{1\perp}/[U_p]^{1/2} < 0.1$ and $0.4 < p_{1\perp}/[U_p]^{1/2} < 0.5$, respectively. In panels (d), (e), and (f), both transverse momenta are confined to the intervals $0 < p_{n\perp}/[U_p]^{1/2} < 0.5$, $0.5 < p_{n\perp}/[U_p]^{1/2} < 1$, and $1 < p_{n\perp}/[U_p]^{1/2} < 1.5$, respectively. Right-hand panels: same as left panels, but for the Coulomb interaction (1.14a). From [17]

Figure 1.6 exhibits some representative results. The two left-hand panels are for the three-body contact interaction (1.14b), the two right-hand panels for the Coulomb interaction (1.14a). A detailed discussion of the results can be found in [17, 18]. In panels (a) the transverse momenta are entirely integrated over, in the remaining panels only partly as specified in the caption. For the Coulomb interaction, we observe its characteristic footprint: one momentum is large while the other one is small. This is a consequence of the form factor of the Coulomb interaction, which is

$$V_{\mathbf{pk}} \sim \frac{1}{(\boldsymbol{p}_1 - \boldsymbol{k})^2[2|E_{02}| + (\boldsymbol{p}_1 + \boldsymbol{p}_2 - \boldsymbol{k} + \boldsymbol{A}(t))^2]^2} + (\boldsymbol{p}_1 \leftrightarrow \boldsymbol{p}_2). \qquad (1.21)$$

Physically, recall that the drift momentum $\boldsymbol{k}$ of the first electron is small [cf. equation (1.11)]. In most cases, since the Coulomb interaction is of long range, it will interact with the bound electron at large distance, so that it will transfer as little momentum as possible to the bound electron. Therefore,

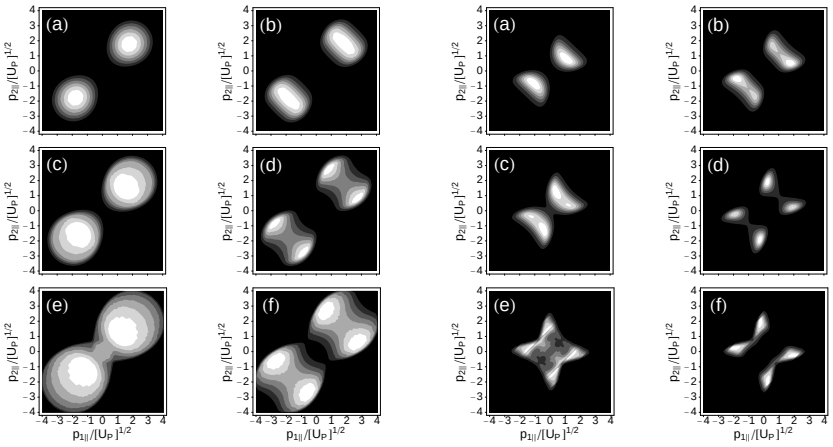

Fig. 1.7. The two left-hand panels: Comparison of the double-ionization correlation densities (1.20) without (left-hand column: panels (a), (c), and (e)) and with (right-hand column: panels (b), (d), and (f)) electron-electron repulsion in the final state. The interaction V_{12} is specified by the three-body contact interaction (1.14b). Parameters are for argon ($E_{01} = 0.58$ a.u., $E_{02} = 1.015$ a.u.), the laser frequency is $\omega = 0.057$ a.u. (Ti:Sa). Panels (a) and (b): $I = 2.5 \times 10^{14}$ Wcm^{-2} ($U_p = 0.54$ a.u), $|\boldsymbol{p}_{1\perp}| \geq 0.5$ a.u.; Ref. [35]; (c) and (d): as before, but with $|\boldsymbol{p}_{1\perp}| \leq 0.5$ a.u.; (e) and (f): $I = 4.7 \times 10^{14}$ Wcm^{-2} ($U_p = 1.0$ a.u), $|\boldsymbol{p}_{1\perp}|$ or $|\boldsymbol{p}_{2\perp}| \leq 0.1$ a.u., Ref. [39]. The two right-hand panels: same as the left-hand panels, but with V_{12} specified by the Coulomb interaction (1.14a). From [18]

its drift momentum, which agrees with the momentum outside the field, will remain low. The second electron, on the other hand, is dislodged into the continuum near a zero of the electric field with low initial momentum. Hence, it will undergo maximal acceleration to a momentum near $2\sqrt{U_p}$. This physical argument is reflected in the form factor (1.21). In passing, we mention that the left-hand panel (d) rather well delineates the classically allowed regime discussed above.

1.4 Final-state interaction

The Coulomb attraction of the electrons in the intermediate state and in the final Volkov states by the ion, as well as the Coulomb repulsion between the two final electrons are missing from the theory developed thus far. A rigorous treatment of the first issue has so far resisted any efforts. It is much easier to deal with the Coulomb repulsion of the two electrons in the final state, depicted in the right-hand panel of figure 1.1, since the product of two Volkov states (1.2) can be extended exactly to incorporate the Coulomb repulsion [22]. This is possible because in the long-wavelength approximation

the laser couples to the sum $\boldsymbol{r}_1+\boldsymbol{r}_2$ of the two electron coordinates while the Coulomb repulsion affects their difference $\boldsymbol{r}=\boldsymbol{r}_1-\boldsymbol{r}_2$ just like in the absence of the laser field. The state reads [22]

$$|\psi^{(\mathrm{V})}_{\boldsymbol{p}_1\boldsymbol{p}_2}(t)\rangle = |\psi^{(\mathrm{V})}_{\boldsymbol{p}_1}(t)\rangle \otimes |\psi^{(\mathrm{V})}_{\boldsymbol{p}_2}(t)\rangle$$
$$\times {}_1F_1(-\mathrm{i}\zeta,1;\mathrm{i}(|\boldsymbol{p}||\boldsymbol{r}|-\boldsymbol{p}\cdot\boldsymbol{r}))\mathrm{e}^{-\pi\zeta/2}\Gamma(1+\mathrm{i}\zeta), \tag{1.22}$$

where $\boldsymbol{p}=(\boldsymbol{p}_1-\boldsymbol{p}_2)/2$, $\zeta=|\boldsymbol{p}_1-\boldsymbol{p}_2|^{-1}$ and ${}_1F_1(a;b;z)$ denotes the confluent hypergeometric function.

Typical results obtained with this state are reproduced in figure 1.7, where the parameters have been chosen so as to allow comparison with published experimental data. As expected, the final-state repulsion causes a suppression of the yield along the diagonal $p_{1\parallel}=p_{2\parallel}$. Remarkably, the very simplest model, the three-body contact interaction (1.14b) without final-state Coulomb repulsion (leftmost column), yields the best description of the data [18].

The correlation of the *transverse momenta* including or not including the final-state repulsion is investigated theoretically and compared with data for argon in [41]. Including the final-state repulsion yields a good description of the electron-electron correlation, but the electron-ion correlation is outside of the model.

1.5 Effect of the initial electron bound states

Another ingredient that can be taken into account in our S-matrix theory are the initial states in which both electrons are bound. If the electron-electron interaction V_{12} is a pure two-body interaction as in (1.14a) or in (1.14d), then the initial bound state $|\psi_0^{(2)}\rangle$ of the second electron will enter the form factor $V_{\boldsymbol{pk}}$ via its Fourier transform, cf. equation (1.18). If, on the other hand, we adopt an effective three-body interaction as in (1.14b) or (1.14d), then $V_{\boldsymbol{pk}}$ is independent of the form of the bound state $|\psi_0^{(2)}\rangle$. The bound state $|\psi_0^{(1)}\rangle$ enters via the form factor (1.7), but its effect is generally small. Since most experiments employ neon and argon as targets, whose outer-shell electrons are bound in $2p$ or $3p$ states, respectively, one would expect that p states yield a more realistic description of the two active electrons for these atoms.

Initial bound states $|\psi_0^{(2)}\rangle$ given by hydrogenic states with quantum numbers n and l affect the form factor $V_{\boldsymbol{pk}}$ via the function [cf. (1.18)].

$$u^{(nl)}(\tilde{\boldsymbol{p}}) \sim \frac{\rho_{nl}(\boldsymbol{p},\boldsymbol{k})}{[2|E_{02}|+\tilde{\mathbf{p}}^2]^{n+1}} + (\boldsymbol{p}_1 \leftrightarrow \boldsymbol{p}_2) \tag{1.23}$$

where $\rho_{1s}=1$, $\rho_{2p}=\tilde{p}$, and $\rho_{3p}=\tilde{p}(\tilde{\boldsymbol{p}}^2-2|E_{02}|)$, with $\tilde{\mathbf{p}}=\mathbf{p}_1+\boldsymbol{p}_2-\boldsymbol{k}+\boldsymbol{A}(t)$.

In figure 1.8 the effect of the initial-state wave functions is explored, for the case where the crucial electron-electron interaction is the two-body Coulomb

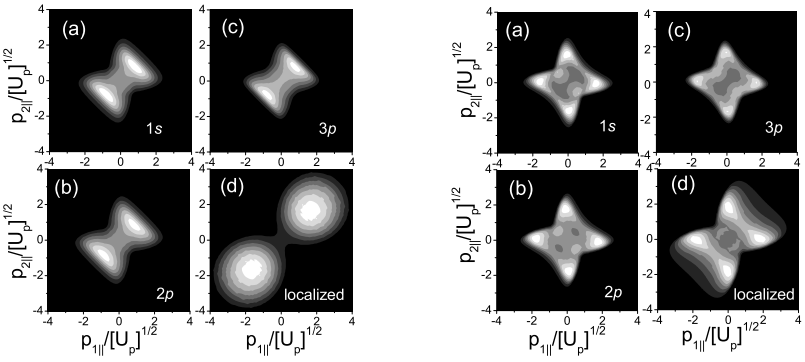

Fig. 1.8. Electron momentum-correlation distributions (1.20) and their dependence on the initial bound state. The left-hand panels (a)-(c) are for the interaction (1.14d) and the right-hand panels (a)-(c) for the interaction (1.14a), for initial $1s$, $2p$, and $3p$ states for both electrons. Panels (d) are for the three-body effective interactions (1.14b) (left) and (1.14c) (right) with the first electron in a $1s$ state. In all situations (even for the $3p$ - state case), the atomic species was taken to be neon ($|E_{01}| = 0.79$ a.u. and $|E_{02}| = 1.51$ a.u.), in order to facilitate a clear assessment of the effects caused by the different initial states. From [27]

interaction (1.14a) and for the case where this interaction is the two-body contact interaction (1.14d), which is not restricted to the position of the ion. In both cases, the form factor includes the function (1.23), which favors momenta such that $p_{1\|} + p_{2\|}$ is large. This is clearly visible for the contact interaction (1.14d) and less so for the Coulomb interaction (1.14a) whose form factor also includes the factor (1.19), which favors $p_{1\|} = 0$ (or $p_{2\|} = 0$). We conclude that (i) the effect of the specific bound state of the second electron is marginal and (ii) that a pure two-body interaction, be it of Coulomb type as in (1.14a) or contact type as in (1.14d), yields a rather poor description of the data. A three-body effective interaction, which only acts if the second electron is positioned at the ion, provides superior results, notably the three-body contact interaction (1.14b), cf. the left-hand panel (d). This points to the significance of the interaction of the electrons with the ion, which so far has not been incorporated into the S-matrix theory beyond the very approximate description via effective three-body interactions such as (1.14b) or (1.14c).

The alternative interpretation [27] mentioned above in section 1.3 assumes that the wave function of the second bound electron is extremely localized near the position of the ion. The labels "localized" in figures 1.8 and 1.10 are motivated by this interpretation.

For exponentially decaying bound states, the form factors $V_{\boldsymbol{k}0}$ are of the form

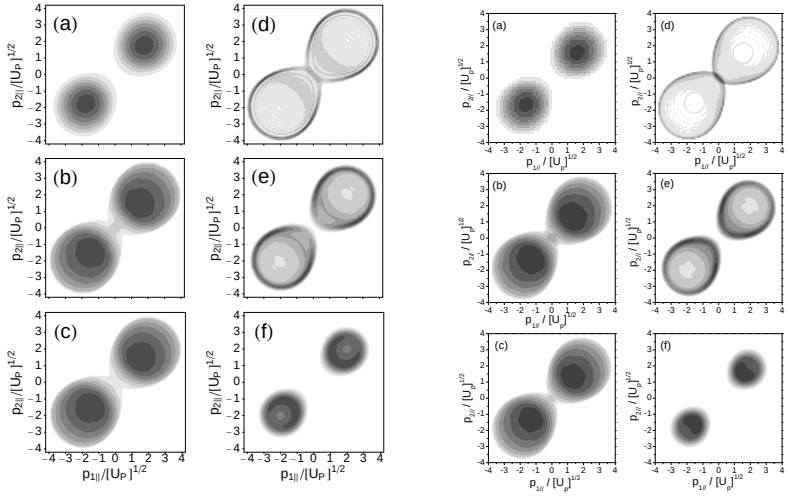

Fig. 1.9. The left-hand panels are identical with the left-hand panels of figure 1.6 where the pertinent parameters are given. They are to be compared with the right-hand panels, which were calculated under the same conditions but from the classical model (1.27) for the contact interaction. Equation (1.29) underlies panel (a)

$$V_{\boldsymbol{k}0} \sim \frac{f(k + A(t'))}{\left([\boldsymbol{k} + \boldsymbol{A}(t')]^2 + 2|E_{01}| \right)^n}, \tag{1.24}$$

where n is an integer number. According to the saddle-point equation (1.8a), the denominator vanishes, so that such form factors are singular. In order to overcome the problem with the bound-state singularity, we take the modified action

$$\tilde{S}(t, t', \boldsymbol{p}_j, \boldsymbol{k}) = S(t, t', \boldsymbol{p}_j, \boldsymbol{k}) - \mathrm{i} \ln [V_{\boldsymbol{k}0}] \tag{1.25}$$

in the transition amplitude (1.4). This leads to modifications in the saddle-point equations (1.8a), and (1.8c) which, physically, determine the tunneling and the return condition. Such modifications depend on the initial bound state of the first electron. We found, however, that they only lead to a minor suppression in the yield, in the region of small parallel momenta (for details cf. [27]).

1.6 The classical limit

The model investigated so far is a *coherent* three-step model, which comprises field-induced tunneling of the first electron out of its binding potential, propagation of this electron in the presence of the laser field, and recollision with the ion leading to second ionization. Of these, only the first step is genuinely

quantum mechanical, while the other two proceed largely classically. The tunneling process is governed by a tunneling rate that is well approximated by the quasi-static limit [42]

$$R(t') \sim |E(t')|^{-1} \exp\left[-2(2|E_{01}|)^{3/2}/(3|E(t')|)\right]. \tag{1.26}$$

Ignoring quantum-mechanical features such as spreading and interference, the essential classical physics then are described by the electron-momentum distribution function [17]

$$\begin{aligned} F(\boldsymbol{p}_1, \boldsymbol{p}_2) &= \int \mathrm{d}t' R(t') \delta\left(\frac{1}{2}\sum_{i=1}^{2}[\boldsymbol{p}_i + \boldsymbol{A}(t)]^2 + |E_{02}| - E_{\mathrm{ret}}(t)\right) |V_{\boldsymbol{pk}}|^2 \\ &= \int \mathrm{d}t' R(t') \delta\left(\frac{1}{2}(\boldsymbol{p}_{1\perp}^2 + \boldsymbol{p}_{2\perp}^2) - \Delta E\right) |V_{\boldsymbol{pk}}|^2 \end{aligned} \tag{1.27}$$

with

$$\Delta E \equiv \Delta E(p_{1\parallel}, p_{2\parallel}, t) \equiv E_{\mathrm{ret}}(t) - |E_{02}| - \frac{1}{2}\sum_{i=1}^{2}[p_{i\parallel} + A(t)]^2. \tag{1.28}$$

This is an integral over the ionization time t'. The rescattering time t, which is a function of t', must be calculated via classical mechanics assuming that the first electron is set free with zero velocity at the time t. The distribution function (1.27) corresponds to a *rate* (not an amplitude), which incorporates the three steps incoherently (multiplicatively): Tunneling is specified by the rate (1.26), and propagation from the ionization time t' to the rescattering time t determines the kinetic energy $E_{\mathrm{ret}}(t)$. Finally, inelastic rescattering is subject to energy conservation (expressed by the δ function) and the momenta are distributed according to the square of the form factor (1.6).

Usually, not all six momentum components $\boldsymbol{p}_1$ and $\boldsymbol{p}_2$ are observed. Those that are not can be integrated over. This is very easily carried out analytically [17] provided the form factor is constant as it is for the three-body contact interaction (1.14b). For example, if only the longitudinal components are observed, the pertinent distribution with the transverse components completely integrated over is

$$\int \mathrm{d}^2\boldsymbol{p}_{1\perp}\mathrm{d}^2\boldsymbol{p}_{2\perp} F(\boldsymbol{p}_1, \boldsymbol{p}_2) = 4\pi^2 \int \mathrm{d}t' R(t')(\Delta E)_+ \tag{1.29}$$

where $x_+ = x\theta(x)$ with $\theta(x)$ the unit step function, and

$$\Delta E \equiv \Delta E(p_{1\parallel}, p_{2\parallel}, t) \equiv E_{\mathrm{ret}}(t) - |E_{02}| - \frac{1}{2}\sum_{i=1}^{2}[p_{i\parallel} + A(t)]^2. \tag{1.30}$$

The outcome of (1.29) along with its quantum-mechanical counterpart are displayed in panels (a) of figure 1.9 for the three-body contact interaction

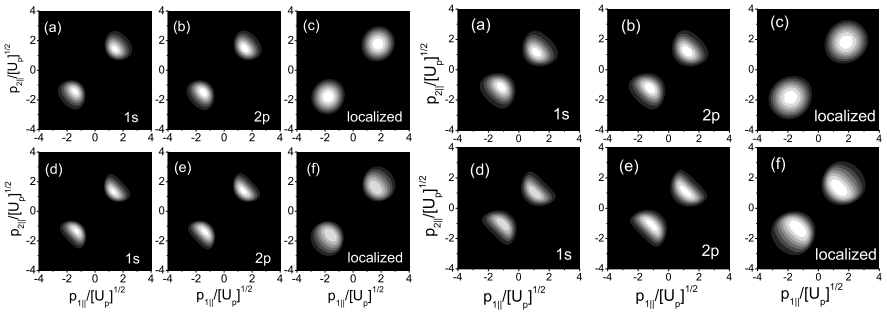

Fig. 1.10. Electron momentum distributions for neon ($|E_{01}| = 0.79$ a.u. and $|E_{02}| = 1.51$ a.u.) subject to a linearly polarized monochromatic field with frequency $\omega = 0.057$ a.u. and intensity $I = 3.0 \times 10^{14}\mathrm{W/cm}^2$, as functions of the electron momentum components parallel to the laser-field polarization. The left and the right panels correspond to the classical and to the quantum-mechanical model, respectively. The upper and lower panels have been computed for a contact and Coulomb-type interaction V_{12}, respectively. In panels (a) and (d), and (b) and (e), the second electron is taken to be initially in a $1s$, and in a $2p$ state, respectively, whereas in panels (c) and (f) the spatial extension of the bound-state wave function has been neglected. The transverse momenta have been integrated over

(1.14b). Both distributions are very similar, apart from minor differences near the boundary of the classically allowed region. This is also true for other forms of the electron-electron interaction V_{12} and initial bound states. In the other panels (b) – (f), the transverse momenta are restricted to certain intervals. Formulas analogous to (1.29) for these situations can be found in [17].

As the intensity decreases, the classical version (1.27) becomes an increasingly poor approximation. Ultimately, at and below the "threshold intensity", when the kinetic energy of the returning electron no longer suffices to free the second electron (i.e., the argument of the δ function never vanishes), the classical distribution becomes identically zero. Figure 1.10 shows an example, for an intensity of roughly 30% above the threshold. Already in this case, the quantum-mechanical distributions are far broader than their classical counter parts. This is due to the fact that the classical model underestimates the yield already near the boundary (and, of course, outside) of the classically allowed regime, which was defined in section 1.2.1. Experiments in this intensity region [34] do not exhibit any significant qualitative change in the ion-momentum distributions when the intensity approaches and passes the threshold intensity. In contrast, the quantum-mechanical ion-momentum distributions decrease quickly in magnitude and become narrowly concentrated about the value (1.12); see figure 1.4.

The S-matrix element (1.1) does not take into account the fact that owing to the presence of the field $E(t)$ the second electron can escape over the saddle formed by the Coulomb field and the scalar potential $zE(t)$ of the

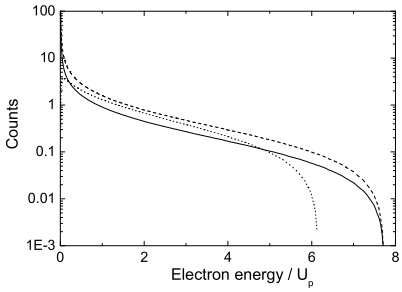

Fig. 1.11. One-electron energy spectra derived in coincidence with double ionization derived from (1.31) for various noble gases. Solid line: He at laser intensity $I = 8 \times 10^{14}\mathrm{W/cm}^2$, dashed line: Ne at $I = 6 \times 10^{14}\mathrm{W/cm}^2$, dotted line: Ar at $I = 2.5 \times 10^{14}\mathrm{W/cm}^2$. The parameters correspond to the experimental data of [51]

laser field [20]. In effect, this lowers the binding energy of the second electron to the value $E_{02}(t) = |E_{02}| - 2\sqrt{2|E(t)|}$. This value can be introduced by hand into the classical distribution (1.27), which thereupon becomes again applicable down to a much lower intensity. This way, fair agreement with the data has been reached [34]. Further discussion of this issue is given in [43].

So long as, however, the driving-field intensity is far above the threshold, the S-matrix amplitude (1.1) and its classical limit (1.27) yield practically identical results. This shows that, in this regime, NSDI is (apart from its initiation via tunneling) an essentially classical phenomenon. This provides a physical justification for extending the classical model to more complex scenarios, such as, for instance, more than two electrons (section 1.8).

The classical model can also be employed to derive one-electron spectra in coincidence with NSDI. For constant form factors (three-body contact interaction), the corresponding expression is [43]

$$\int \mathrm{d}^3\boldsymbol{p}_2 F(\boldsymbol{p}_1, \boldsymbol{p}_2) = 4\pi\sqrt{2} \int \mathrm{d}t' R(t') \, (\Delta E_1)_+^{1/2} \tag{1.31}$$

with $\Delta E_1 \equiv E_{\mathrm{ret}}(t) - |E_{02}| - \frac{1}{2}[\boldsymbol{p}_1 + \boldsymbol{A}(t)]^2$. An example is presented in figure 1.11.

1.7 NSDI by few-cycle laser pulses

In the results discussed so far, the external laser field has been approximated by a monochromatic plane wave. This is a reasonable approximation for pulses with a length down to, say, eight cycles, which covers most NSDI experiments. Recently, however, laser pulses of only a few cycles' length have become the tools of choice in laser-atom physics [44].

A few-cycle (n-cycle) pulse can be described by the vector potential

$$\boldsymbol{A}(t) = A_0 F(t) \sin(\omega t + \phi) \boldsymbol{e}_x, \tag{1.32}$$

where the positive definite envelope $F(t)$ ($0 \leq F(t) \leq 1$) is zero outside the interval $0 \leq t \leq nT$ ($T = 2\pi/\omega$) and assumes its maximum at $t = nT/2$. The specific pulse shape is determined by the carrier-envelope (CE) phase ϕ, which specifies the offset between the envelope of the pulse and its "carrier wave" with frequency ω. Below, for the explicit results, we will use $F(t) = \exp[-4(\omega t - \pi n)^2/(\pi n)^2]$.

When a few-cycle pulse interacts with matter, the resulting effects strongly depend on the value of the CE phase. For example, above-threshold ionization spectra lose the backward-forward symmetry ($\boldsymbol{p} \rightarrow -\boldsymbol{p}$), which they obey for monochromatic fields. This is particularly pronounced in their high-energy part, which is caused by rescattering [45]. Indeed, this effect is being utilized for the measurement of the CE phase. NSDI, to the extent that is due to rescattering, can be expected also to react very sensitively to any change in the CE phase. Indeed, it has been shown that the momentum correlation distribution of NSDI can exhibit dramatic changes upon a small variation of the CE phase [46, 47].

Figure 1.12 exhibits NSDI electron-momentum-correlation distributions calculated for a 4-cycle pulse having the shape (1.32). Unlike the corresponding distributions for a long pulse shown in figures 1.6 – 1.10, which are without exception symmetric with respect to the antidiagonal $[(p_{1\parallel}, p_{2\parallel}) \rightarrow -(p_{1\parallel}, p_{2\parallel})]$, the distributions of figure 1.12 are, in general, unequally concentrated in the regions of either positive or negative momenta. Upon a critical value of the CE phase, the distributions shift from one region to the other and, for increasing intensity, the CE phase for which the distribution starts to spill over from the first to the third quadrant, moves to smaller values. This behavior is obtained both from the quantum-mechanical S-matrix amplitude (1.1) (left-hand panels), and from its classical limit (1.27) (right-hand panels). (Due to its very good agreement with the experiments in the long-pulse case, we employed the three-body-contact interaction (1.14b) in both calculations.) Minor differences are only observed at the boundary of the classically allowed region, or at the CE phases for which the momenta start to change sign. As observed before, the agreement between the quantum-mechanical and the classical calculations improves for increasing intensity.

The dependence of the yields on the absolute phase can be explained by a change in the dominant set of orbits of the first-ionized electron rescattering inelastically off its parent ion. For an orbit to make an important contribution, two conditions must be satisfied: first, the probability that the electron tunnel out at a time t' must not be too small[6] and, second, the subsequent

[6] In the classical and quantum-mechanical frameworks, this probability is related to the quasi-static rate $R(t')$ or to the imaginary part $\mathrm{Im}\, t'$, respectively. For details cf. [47].

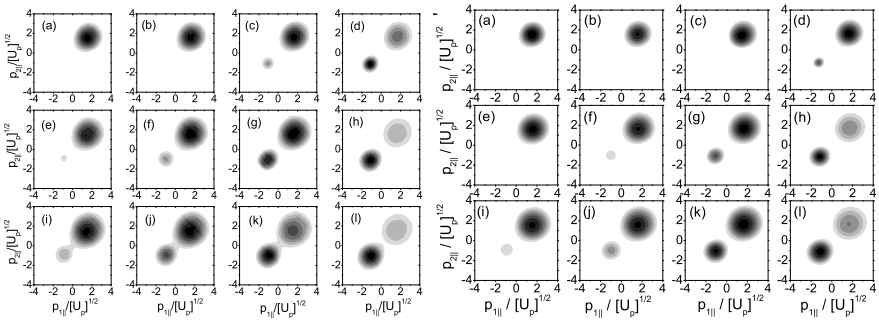

Fig. 1.12. Electron momentum distributions computed for neon ($|E_{01}| = 0.79$ a.u. and $|E_{02}| = 1.51$ a.u.) subject to a four-cycle pulse ($n = 4$) of frequency $\omega = 0.057$ a.u, for various intensities and CE phases. The four left-hand panels and the four right panels correspond to the quantum-mechanical and to the classical computation, respectively. The upper, middle, and lower rows are for $I = 4 \times 10^{14}\mathrm{W/cm}^2 (U_p = 0.879$ a.u), $I = 5.5 \times 10^{14}\mathrm{W/cm}^2 (U_p = 1.2$ a.u), and $I = 8 \times 10^{14}\mathrm{W/cm}^2 (U_p = 1.758$ a.u), respectively. The CE phases are given as follows: Panels (a), (e) and (i): $\phi = 0.8\pi$; panels (b), (f) and (j): $\phi = 0.9\pi$; panels (c), (g) and (k): $\phi = 1.0\pi$; and panels (d), (h) and (l): $\phi = 1.1\pi$. From [47]

acceleration must be strong enough that the electron return to the ion (at the time t) with sufficient kinetic energy $E_{\mathrm{ret}}(t)$. These two conditions reduce the significance of start times within the trailing part of the pulse ($t' \geq nT/2$).

Both in the quantum-mechanical and in the classical calculations, only the first return of the electron to the ion has been considered. Due to wave function spreading, the contributions of the longer orbits are suppressed. The most remarkable result of these investigations is the surprisingly high sensitivity of the $(p_{1\parallel}, p_{2\parallel})$-momentum distribution to variations of the CE phase. In principle, this lends itself to a very precise determination and control of this parameter.

The features discussed above have been observed in recent NSDI experiments, for argon irradiated by few-cycle pulses. The experimental findings exhibit very good agreement with the theory. In particular, the shift of the $(p_{1\parallel}, p_{2\parallel})$ distribution from the first to the third quadrant takes place around the predicted critical phases [48].

1.8 Nonsequential multiple ionization

If the kinetic energy $E_{\mathrm{ret}}(t)$ of the returning electron is sufficiently high, it may as well free more than one bound electron in a single nonsequential coherent process. The signature of such a recollision–impact nonsequential multiple ionization (NSMI) process will be a large momentum of the multiply charged ion, around the value (1.12) with the factor of 4 replaced by $2N$

for N-fold NSMI. The underlying argument is in complete analogy with the one given above in connection with (1.12). Indeed, NS3I of neon was observed several years ago [4], and extensive measurements of NS3I and NS4I of neon and argon were published recently [49]. The data for neon do display the characteristic hump in the distribution of the ion-momentum component parallel to the laser field at a value compatible with the afore-mentioned estimate.

An ab-initio description of NSMI appears to be all but impossible. In the S-matrix context, the single Feynman diagram of figure 1.1(a) is replaced by a large number of more complicated diagrams: to establish contact between N electrons requires a minimum of $N-1$ two-particle interactions, and this entails $N-2$ internal electron propagators (for NSDI there was none). Moreover, based on the experience gained from NSDI, it appears likely that some interaction with the ion has to be included for a realistic description, which increases the number of diagrams as well as their complexity. Hence, while an extension of the quantum-mechanical amplitude (1.1) to triple and higher nonsequential ionization, maintaining two-body electron-electron interactions to be responsible for the energy exchange, appears not to be practically feasible, an extension of the classical distribution function (1.27) is near at hand. We consider a statistical description where the first-ionized electron returning to its parent ion at time t shares its energy with $N-1$ up to this time bound and inactive electrons merely according to the available phase space, without any dynamical bias. We do not attempt to model *how* this is accomplished, presumably through many repeated electron-electron and electron-ion interactions. We do assume, however, that this energy-sharing process requires some time so that the electrons are freed at the time $t+\Delta t$ rather than the return time t. Comparable statistical models have been used in many areas of physics whenever the detailed dynamics were unknown or too complicated; see, e.g. [50].

Then, the distribution of the final electron momenta $\boldsymbol{p}_n$ $(n=1,...,N)$ is given by [52]

$$F(\boldsymbol{p}_1,\ldots,\boldsymbol{p}_N)=\int \mathrm{d}t' R(t')\delta\left(E_0^{(N)}-E_{\mathrm{ret}}(t)+\frac{1}{2}\sum_{n=1}^{N}[\boldsymbol{p}_n+\boldsymbol{A}(t+\Delta t)]^2\right), \tag{1.33}$$

where $E_0^{(N)}=\sum_{n=2}^{N}|E_{0n}|$ is the total energy necessary to remove the $N-1$ bound electrons. Compared with (1.27), the time delay Δt is a new feature. It is the sum of a "thermalization time" – the time it takes for the N electrons to reach an energy distribution governed only by phase space, without any memory of the distribution at the time t when the returning electron had all the energy – and a possible additional "dwell time" before all electrons start leaving the vicinity of the ion. The corresponding distribution for the parallel ion momentum $P_{\parallel}$ can be obtained from (1.33) in analogy with (1.13), cf. also [52]. It is

$$F_{\rm ion}(P_\parallel) \equiv \int {\rm d}^2\boldsymbol{p}_\perp F_{\rm ion}(\boldsymbol{p}) \sim \int {\rm d}t' R(t') \left(\Delta E_{{\rm ion}\parallel}\right)_+^{\frac{3N}{2}-\frac{3}{2}}, \qquad (1.34)$$

where $\Delta E_{{\rm ion}\parallel} \equiv E_{\rm ret}(t) - E_0^{(N)} - \frac{1}{2N}[P_\parallel - NA(t+\Delta t)]^2$.

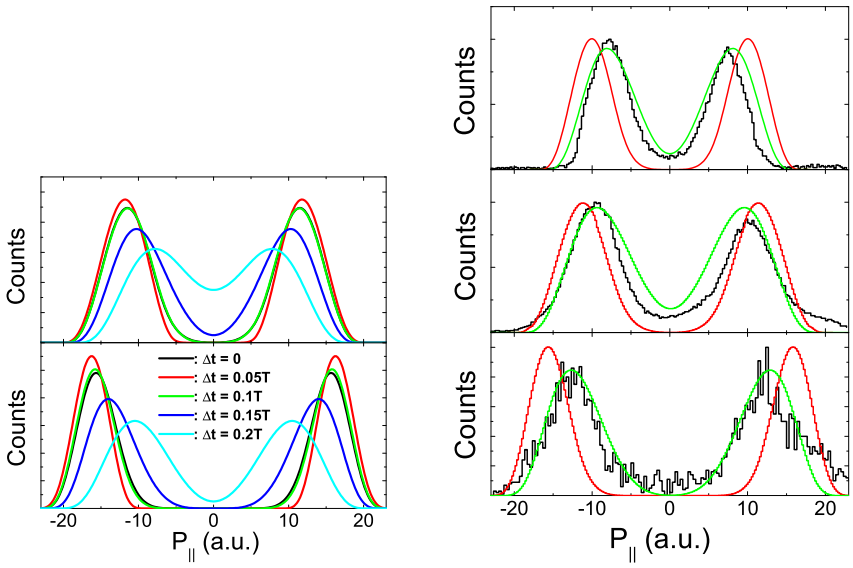

Fig. 1.13. Left Panels: Distribution of the longitudinal ion momentum for triple (upper panel) and quadruple (lower panel) nonsequential ionization of neon at $2\,{\rm PWcm}^{-2}$ calculated from Eq. (1.34) for various delays Δt as indicated in the lower panel. Note that in the upper panel the curves for $\Delta t = 0$ and $\Delta t = 0.1T$ almost completely overlap. Right panels: Distribution of the longitudinal momentum of nonsequential triple ionization of neon at 1.5 ${\rm PWcm}^{-2}$ (upper panel), $2.0\,{\rm PWcm}^{-2}$ (middle panel), and of nonsequential quadruple ionization of Ne at $2.0\,{\rm PWcm}^{-2}$ (lower panel). The rugged (black) curves represent the data of Fig. 2 of Ref. [49]. The outermost smooth (red) curve and the innermost smooth (green) curve are calculated from (1.34) for $\Delta t = 0$ and $\Delta t = 0.17T$. From [52]

In figure 1.13, we display such distributions for Ne^{3+} and Ne^{4+} and compare with the experimental data [49]. The time delay Δt between the recollision of the first electron and the time when all N electrons leave the ion influences both the width and the peaks of the momentum distributions. This is expected since, by introducing a time delay, one is shifting the center of the hypersphere in the $(\boldsymbol{p}_1, ..., \boldsymbol{p}_N)$ space, which delimits the region for which nonsequential multiple ionization is energetically allowed. Specifically, for longer delays, the distributions broaden considerably, and the peak momenta are displaced towards lower values. Optimal results regarding the

widths and centers of the momentum distributions are obtained if the time delay is $\Delta t \simeq 0.17T$, where T is the driving-field cycle. For a Ti:Sa laser with $T \approx 2.7\,\mathrm{fs}$, this yields an upper bound for the thermalization time of roughly 460 as.

This simple statistical model is compatible, for the case of neon, with the data available thus far. Moreover, it allows one to infer a value of the thermalization time. This value comes out to be in the attosecond regime. In principle, such bounds can be made even tighter by reducing the widths of the electron-momentum distributions. This can be done by limiting the temporal range of return times for the first electron using, for instance, an additional perpendicularly polarized driving wave at twice the frequency.

1.9 Conclusions

The fully differential cross sections currently recorded with the help of the reaction microscope pose an enormous challenge to theory. Calculations from first principles are only possible for helium, if at all. In this paper, we have surveyed S-matrix methods that implement the rescattering–impact-ionization scenario in the two-electron context, strictly speaking for helium only. Even in this simplest case, the electron interaction with the ion is neglected. We have then discussed attempts, making a virtue out of necessity, at re-interpreting the two-particle electron-electron interaction as an effective interaction that includes the presence of the ion. The fact that, at least in the case of neon, a three-body contact interaction yields a fair description of the existing data (and also agrees well with classical-trajectory simulations [11]) remains a puzzle that calls for an explanation.

Nonsequential double and multiple ionization are to a large part classical phenomena. Indeed, the S-matrix approach suggests a pertinent classical limit. We have summarized evidence that the latter reproduces the fully quantum-mechanical results very well in parameter regions where this can be expected. Finally, we have extended such classical avenues to a statitical description of nonsequential triple and quadruple ionization. For reasons not currently understood, again this yields a fair description of the data available for neon. While a more microscopic description of these extremely involved phenomena lies in the future, we believe that the simple models summarized in this paper will remain valuable as benchmark results.

References

1. A. l'Huillier, L.A. Lompré, G. Mainfray, C. Manus: Phys. Rev. A **27**, 2503 (1983)
2. R. Dörner, Th. Weber, M. Weckenbrock, A. Staudte, M. Hattas, H. Schmidt-Böcking, R. Moshammer, J. Ullrich: Adv. At., Mol., Opt. Phys. **48**, 1 (2002); A. Becker, R. Dörner, R. Moshammer: J. Phys. B **38**, S753 (2005)

3. Th. Weber, M. Weckenbrock, A. Staudte, L. Spielberger, O. Jagutzki, V. Mergel, F. Afaneh, G. Urbasch, M. Vollmer, H. Giessen, R. Dörner: Phys. Rev. Lett. **84**, 443 (2000); Th. Weber, H. Giessen, M. Weckenbrock, G. Urbasch, A. Staudte, L. Spielberger, O. Jagutzki, V. Mergel, M. Vollmer, and R. Dörner: Nature (London) **405**, 658 (2000)
4. R. Moshammer, B. Feuerstein, W. Schmitt, A. Dorn, C.D. Schröter, J. Ullrich, H. Rottke, C. Trump, M. Wittmann, G. Korn, K. Hoffmann, W. Sandner: Phys. Rev. Lett. **84**, 447 (2000)
5. B. Feuerstein, R. Moshammer, D. Fischer, A. Dorn, C.D. Schröter, J. Deipenwisch, J.R. Crespo Lopez-Urrutia, C. Höhr, P. Neumayer, J. Ullrich, H. Rottke, C. Trump, M. Wittmann, G. Korn, and W. Sandner: Phys. Rev. Lett. **87**, 043003 (2001)
6. P.B. Corkum: Phys. Rev. Lett. **71**, 1994 (1993)
7. M. Weckenbrock, D. Zeidler, A. Staudte, Th. Weber, M. Schöffler, M. Meckel, S. Kammer, M. Smolarski, O. Jagutzki, V.R. Bhardwaj, D.M. Rayner, D.M. Villeneuve, P.B. Corkum, R. Dörner: Phys. Rev. Lett. **92**, 213002 (2004)
8. H. Niikura, F. Légaré, R. Hasbani, M.Yu. Ivanov, D.M. Villeneuve, P.B. Corkum: Nature (London) **417**, 917 (2002)
9. R. Panfili, S.L. Haan, J.H. Eberly: Phys. Rev. Lett. **89**, 113001 (2002); S.L. Haan, P.S. Wheeler, R. Panfili, J.H. Eberly: Phys. Rev. A **66**, 061402(R) (2002); M. Lein, E.K.U. Gross, V. Engel: Phys. Rev. Lett. **85**, 4707 (2000)
10. D. Dundas, K.T. Taylor, J.S. Parker, E.S. Smyth: J. Phys. B **32**, L231 (1999); J.S. Parker, L.R. Moore, K.J. Meharg, D. Dundas, K.T. Taylor: J. Phys. B **34**, L69 (2001); H.G. Muller: Opt. Express **8**, 425 (2001)
11. J. Chen, J. Liu, L.B. Fu, W.M. Zheng: Phys. Rev. A **63**, 011404(R) (2000); J. Chen, C.H. Nam: Phys. Rev. A **66**, 053415 (2002)
12. A. Becker, F.H.M. Faisal: J. Phys. B **29**, L197 (1996)
13. A. Becker, F.H.M. Faisal: J. Phys. B **38**, R1 (2005)
14. A. Becker, F.H.M. Faisal: Phys. Rev. Lett. **84**, 3546 (2000); *ibid* **89**, 193003 (2002)
15. R. Kopold, W. Becker, H. Rottke, W. Sandner: Phys. Rev. Lett. **85**, 3781 (2000)
16. S.V. Popruzhenko, S.P. Goreslavskii: J. Phys. B **34**, L239 (2001); S.P. Goreslavski, S.V. Popruzhenko: Opt. Express **8**, 395 (2001)
17. C. Figueira de Morisson Faria, H. Schomerus, X. Liu, W. Becker: Phys. Rev. A **69**, 043405 (2004)
18. C. Figueira de Morisson Faria, X. Liu, W. Becker, H. Schomerus: Phys. Rev. A **69**, 012402(R)(2004)
19. C. Ruiz, L. Plaja, L. Roso: Phys. Rev. Lett. **94**, 063002 (2005)
20. H.W. van der Hart, K. Burnett: Phys. Rev. A **62** 013407 (2000)
21. D.M. Volkov: Zs. Phys. **94**, 250 (1935)
22. F.H.M. Faisal: Phys. Lett. A **187**, 189 (1994); A. Becker, F.H.M. Faisal: Phys. Rev. A **50**, 3256 (1994)
23. L.V. Keldysh: Zh. Eksp. Teor. Fiz. **47**, 1945 (1964) [Sov. Phys. JETP **20**, 1307 (1965)]
24. F.H.M. Faisal: J. Phys. B **6**, L89 (1973); H.R. Reiss: Phys. Rev. A **22**, 1786 (1980)
25. M. Lewenstein, Ph. Balcou, M.Yu. Ivanov, A. l'Huillier, P.B. Corkum: Phys. Rev. A **49**, 2117 (1994)
26. S.P. Goreslavskii, Ph.A. Korneev, S.V. Popruzhenko, R. Kopold, W. Becker: J. Mod. Opt. **50**, 423 (2003)

27. C. Figueira de Morisson Faria, M. Lewenstein: J. Phys. B **38**, 3251 (2005)
28. C. Figueira de Morisson Faria, W. Becker: Laser Phys. **13**, 1196 (2003)
29. S.V. Popruzhenko, Ph.A. Korneev, S.P. Goreslavskii, W. Becker: Phys. Rev. Lett. **89**, 023001 (2002)
30. C. Figueira de Morisson Faria, H. Schomerus, W. Becker: Phys. Rev. A **66**, 043413 (2002)
31. D.B. Milošević, W. Becker: Phys. Rev. A **68**, 065401 (2003)
32. D. Bauer, D.B. Milošević, W. Becker: Phys. Rev. A **72**, 023415 (2005)
33. M.V. Frolov, N.L. Manakov, E.A. Pronin, A.F. Starace: Phys. Rev. Lett. **91**, 053003 (2003)
34. E. Eremina, X. Liu, H. Rottke, W. Sandner, A. Dreischuh, F. Lindner, F. Grasbon, G.G. Paulus, H. Walther, R. Moshammer, B. Feuerstein, J. Ullrich: J. Phys. B **36** 3269 (2003)
35. R. Moshammer, B. Feuerstein, J. Crespo López-Urrutia, J. Deipenwisch, A. Dorn, D. Fischer, C. Höhr, P. Neumayer, C.D. Schröter, J. Ullrich, H. Rottke, C. Trump, M. Wittmann, G. Korn, W. Sandner: Phys. Rev. A **65**, 035401 (2002)
36. V.L.B. de Jesus, B. Feuerstein, K. Zrost, D. Fischer, A. Rudenko, F. Afaneh, C.D. Schröter, R. Moshammer, J. Ullrich: J. Phys. B **37**, L161 (2004)
37. U. Eichmann, M. Dörr, H. Maeda, W. Becker, W. Sandner: Phys. Rev. Lett. **84**, 3550 (2000)
38. B.A. Zon: JETP **89**, 219 (1999)
39. M. Weckenbrock, M. Hattass, A. Czasch, O. Jagutzki, L. Schmidt, T. Weber, H. Roskos, T. Löffler, M. Thomson, and R. Dörner: J. Phys. B **34**, L449 (2001)
40. S.P. Goreslavskii, S.V. Popruzhenko, R. Kopold, W. Becker: Phys. Rev. A **64**, 053402 (2001)
41. M. Weckenbrock, A. Becker, A. Staudte, S. Kammer, M. Smolarski, V.R. Bhardwaj, D.M. Rayner, D.M. Villeneuve, P.B. Corkum, R. Dörner: Phys. Rev. Lett. **91**, 123004 (2003)
42. L.D. Landau and E.M. Lifshitz, *Quantum Mechanics* (Pergamon Press, 1977)
43. C. Figueira de Morisson Faria, X. Liu, W. Becker: J. Mod. Opt. (in press)
44. T. Brabec, F. Krausz: Rev. Mod. Phys. **72**, 545 (2000)
45. G.G. Paulus, F. Lindner, H. Walther, A. Baltuška, E. Goulielmakis, M. Lezius, F. Krausz: Phys. Rev. Lett. **91**, 253004 (2003)
46. X. Liu, C. Figueira de Morisson Faria: Phys. Rev. Lett. **92**, 133006 (2004)
47. C. Figueira de Morisson Faria, X. Liu, A. Sanpera M. Lewenstein: Phys. Rev. A **70**, 043406 (2004)
48. X. Liu, H. Rottke, E. Eremina, W. Sandner, E. Goulielmakis, K.O. Keeffe, M. Lezius, F. Krausz, F. Lindner, M.G. Schätzel, G.G. Paulus, H. Walther: Phys. Rev. Lett. **93**, 263001 (2004)
49. A. Rudenko, K. Zrost, B. Feuerstein, V.L.B. de Jesus, C.D. Schröter, R. Moshammer, J. Ullrich: Phys. Rev. Lett. **93**, 253001 (2004)
50. See, e.g., W. Forst: *Theory of Unimolecular Reactions* (Academic Press, New York, 1973); P.J. Robinson and K.A. Holbrook: *Unimolecular Reactions* (Wiley-Interscience, New York, 1972); R. Hagedorn: Nuovo Cimento Suppl. **3**, 147 (1965)
51. J.L. Chaloupka, R. Lafon, L.F. DiMauro, P. Agostini, K.C. Kulander: Opt. Express **8**, 352 (2001)
52. X. Liu, C. Figueira de Morisson Faria, W. Becker, P.B. Corkum: physics/0506187